Nano-waveguide enhanced photothermal interferometry spectroscopy

Yun Qi, Fan Yang, Yuechuan Lin, Wei Jin, *Senior Member, IEEE*, and Hoi Lut Ho

***Abstract*—We report a new optical nano-waveguide enhanced photothermal (PT) interferometry spectroscopy method for trace molecule detection. Absorption of pump evanescent field of an optical nano-waveguide heats up the trace molecules surrounding the waveguide, causing the temperature of waveguide to rise via thermal conduction and modulating the refractive index and dimension of the nano-waveguide. The phase of a probe beam propagating through the same nano-waveguide is then modulated and can be detected with optic fiber interferometry. Numerical simulation with silica, cyclic transparent optical polymer and silicon nano-waveguides with proper dimensions can achieve PT index modulation of 10 to over 8000 times that of the commercial HC-1550-02 photonic bandgap fiber. Experiments with 12-mm-long, 800-nm-diamter silica nanofiber demonstrated a lower detection limit of 600 parts per billion (ppb) acetylene at ambient conditions.**

***Index Terms*—Fiber optics, Optical sensors, Photothermal effects, Optical waveguides.**

I. Introduction

TRACE gas detection is important for environmental protection and industrial control applications. Compared with direct absorption spectroscopy, photothermal interferometry (PTI) spectroscopy has been proven to be a substantially more sensitive technique [1]. PTI spectroscopy typically uses a pump-probe configuration: absorption of a modulated pump heats up the gas sample, changes its refractive index (RI), and modulates the phase of a probe beam propagating through the same gas sample. Free-space PTI systems with high-power pump lasers operating in the mid to far infrared wavelength region have demonstrated ppb (parts per billion) level detection limit [2-4]. Recently, we demonstrated hollow-core photonic crystal fiber (HC-PCF) enhanced PTI spectroscopy for high-sensitivity gas detection. The small mode-field-diameter and low loss of the HC-PCFs enables much higher pump intensity over the free-space systems (for the same power level) as well as longer interaction length. This enhances the photothermal (PT) phase modulation by several orders of magnitude and allows ppb level gas detection with all-fiber systems operating at the telecom near infrared region where the molecular absorption is much weaker [5-7].

This work was supported by the Hong Kong SAR government through GRF grant PolyU 152064/14E, Natural Science Foundation of China through NSFC grants 61535004 and 61290313, and the Hong Kong Polytechnic University through grants 4BCBE, 1-ZVG4, and 4-BCD1 *(Corresponding author: Wei Jin)*.

The authors are from the Department of Electrical Engineering, The Hong Kong Polytechnic University, Kowloon, Hong Kong, China (E-mail: yun.qi@connect.polyu.hk; ee.yangfan@connect.polyu.hk; lin.yuechuan@connect.polyu.hk; ewjin@polyu.edu.hk; eehlho@polyu.edu.hk)

However, in both the free-space and the HC-PCF enhanced PTI systems, the magnitude of PT phase modulation is primarily determined by thermo-optic properties of the gas sample itself, as governed by the Clausius-Mossotti equation [8]. Due to the small thermo-optic coefficient (TOC) of air (about $-10^{-6}\mathrm{K}^{-1}$ at room temperature), the magnitude of PT phase modulation is limited. We here report a nano-waveguide enhanced PTI spectroscopy method that surpasses the limitation set by the thermal and optical properties of the gas sample. By properly selecting the material and dimension of the nano-waveguide, the PT phase modulation per unit length can be made orders of magnitude higher than that in a HC-PCF, enabling higher sensitivity trace molecular detection with more compact sensing devices.

II. Method

The basics of nano-waveguide enhanced PTI spectroscopy may be explained with the aid of Fig. 1. A pump beam propagating in a nanoscale waveguide has a significant portion of evanescent field in air [9, 10], as shown in Fig. 1 (a). Absorption of this evanescent field by the trace molecules heats up the surrounding gas and changes the temperature of gas and the waveguide via thermal conduction. This modulates the refractive index (RI) of the surrounding gas and the waveguide material, as well as the waveguide dimensions, as shown in Fig. 1 (b). If a probe beam is propagating in the same waveguide,

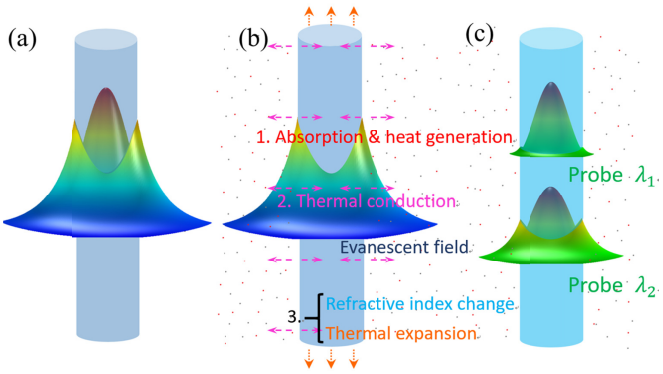

Fig. 1. Basics of nano-waveguide enhanced PTI spectroscopy. (a) Intensity profile of a pump beam propagating in a nano-waveguide. The mode field area of the fundamental waveguide mode can be much smaller and the intensity of the evanescent field near the waveguide surface significantly higher than in a HC-PCF for the same pump power level. (b) Heat generation and conduction, RI change due to thermal-optic effect, and waveguide geometry change due to thermal expansion effect. (c) Probe intensity profiles for two different wavelengths ($\lambda_1<\lambda_2$). The magnitude of PT phase modulation depends on the probe wavelength due to different overlaps of the probe field with the nano-waveguide.

the phase of the probe will be modulated. Compared with traditional PTI methods, the introduction of a nanoscale optical waveguide brings extra degrees of freedom to dramatically enhance the PT phase modulation by selecting proper waveguide materials and transverse dimensions in relation to the pump and probe wavelengths.

The change of temperature distribution in the nano-waveguide as well as the surrounding air is governed by the following equations [11]:

$$\rho_a C_a \frac{\partial T}{\partial t} + \nabla \cdot (-k_a \nabla T) + \rho_a C_a \vec{u} \cdot \nabla T = \alpha c P_{pump} I_{nom-eva}(r,\theta) g(t) \quad (1)$$

$$\rho_w C_w \frac{\partial T}{\partial t} + \nabla \cdot (-k_w \nabla T) = 0 \quad (2)$$

Equations (1) and (2) describe the heat transfer in air and the nano-waveguide respectively. The right hand side of Equation (1) is the heat source with α, c, P_{pump}, $I_{nom-eva}(r,\theta)$ and $g(t)$ representing respectively the absorption coefficient, trace gas concentration, peak pump power level, normalized evanescent-field intensity distribution of the pump as a function of radius r and azimuth angle θ, and the time-domain waveform of the modulated pump. ρ_a, C_a, k_a and $\vec{u}$ are respectively the density, heat capacity, heat conductivity and velocity field of surrounding air. ρ_w, C_w and k_w are respectively the density, heat capacity and heat conductivity of the waveguide material. By solving Equations (1) and (2), the temperature distribution $T_a(r,\theta,t)$ in the surrounding air and $T_w(r,\theta,t)$ in the nano-waveguide can be obtained and the RI change in air and the nano-waveguide may be obtained by using:

$$n_a(r,\theta,t) = [T_a(r,\theta,t) - T_0]\frac{dn_a}{dT} + n_{a0} \quad (3)$$

$$n_w(r,\theta,t) = [T_w(r,\theta,t) - T_0]\frac{dn_w}{dT} + n_{w0} \quad (4)$$

where dn_a/dT, dn_w/dT, n_{a0} and n_{w0} are the TOCs and initial RIs of air and waveguide material respectively. T_0 is the initial temperature and is considered the same in the surrounding air and the nano-waveguide. The change of the effective mode index of the probe beam can then be expressed as:

$$\Delta n_{eff}(t) = n_{eff}\left[n_w(r,\theta,t), n_a(r,\theta,t), \lambda_{probe}, S(r,\theta)\right] - n_{eff0} \quad (5)$$

where $S(r,\theta)$ is the transverse cross-sectional shape of the nano-waveguide and n_{eff0} is the initial effective mode index. Although the temperature change would also modulate $S(r,\theta)$, which in turn influences the n_{eff}, but its effect is comparably much smaller and may be neglected. Equations (1), (2) and (5) can be solved numerically by using finite element method (e.g. COMSOL Multiphysics) and the effective mode index change can then be obtained. The temperature change also modulates the length of the waveguide:

$$\Delta L(t) = L(t) - L_0 = L_0 e_w \Delta T_w(t) \quad (6)$$

where, L_0 and e_w is the initial length and the thermal expansion coefficient (TEC) of the waveguide material. Combining equations (5) and (6), the PT phase modulation of the probe beam propagating through the nano-waveguide may be expressed as:

$$\Delta\varphi(t) = \frac{2\pi}{\lambda_{probe}}\left[\Delta n_{eff}(t) L_0 + \overline{n}_{eff}\Delta L(t)\right] = \frac{2\pi}{\lambda_{probe}} L_0\left[\Delta n_{eff}(t) + \overline{n}_{eff} e_w \Delta T_w(t)\right] \quad (7)$$

We here define, respectively, the first and second terms in the bracket in the second-row of Equation (7) as equivalent RI modulations due to thermo-optic effect (TOE) and thermal expansion effect (TEE), and the sum of them is the total equivalent RI modulation. Fig. 2 summarizes the processes and the main effects that determine the magnitude of the PT phase modulation. As will be shown in the next section, the pump intensity near the surface of the nano-waveguide, the TOE of waveguide material and the TEE of the nano-waveguide are the three main factors (marked in blue in Fig. 2) that could bring tremendous enhancement to PT phase modulation over the traditional free-space and HC-PCF PTI systems.

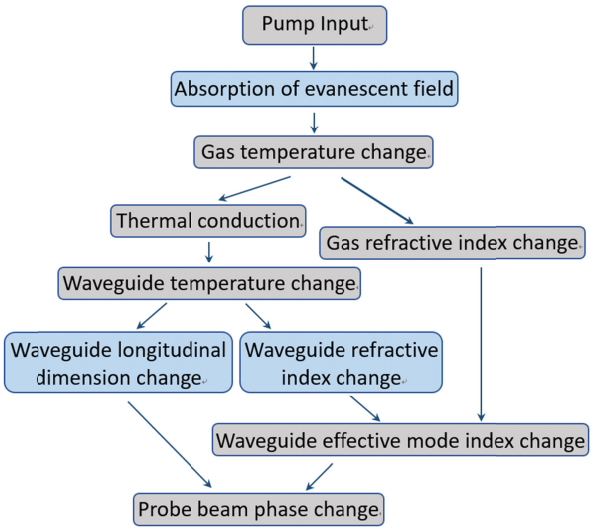

Fig. 2. Process and the main effects involved in the generation of probe phase modulation. The large field intensity of the pump around a nano-waveguide, coupled with a waveguide material with large TOC and TEC as well as a proper probe wavelength enable significant enhancement of PT phase modulation.

III. Numerical Simulations

The potential of the proposed nano-waveguide enhanced PTI spectroscopy is demonstrated by numerical simulations for three different types of waveguides made of silica, cyclic transparent optical polymer (CYTOP) and silicon, respectively. The thermal and optical properties of the three types of materials are summarized in TABLE I. Simulations were conducted by assuming a sample gas of 10^4 parts-per-million (ppm) of acetylene balanced by nitrogen, a pump power of 40 mW and a pump modulation waveform of $g(t) = 0.5 \cdot [1 + sin(2\pi \cdot freq \cdot t)]$. For silica and CYTOP waveguides, the cross-sectional shapes of the waveguides are assumed to be circular and the pump wavelength is 1532.83 nm, corresponding to the P(13) line of

acetylene (vibrational band $v_1 + v_3$ with rotational transition $J' = 12$ to $J'' = 13$) with an absorption coefficient of $\alpha = 1.051\ \mathrm{cm}^{-1}$ for pure acetylene at standard pressure and temperature. For silicon waveguide, the cross-sectional shape is rectangular and the pump wavelength is assumed to be $3025.75\ \mathrm{nm}$, corresponding to the R(9) absorption line of acetylene (vibrational band v_3 with rotational transition $J' = 10$ to $J'' = 9$) with an absorption coefficient of $\alpha = 24.07\ \mathrm{cm}^{-1}$ for pure acetylene. What is worth mentioning is that for the heat transfer equation (1), the thermal convection term $\rho_a C_a \vec{u} \cdot \nabla T$ contributes much smaller than the thermal conduction term $\nabla \cdot (-k_a \nabla T)$ [8]. So equation (1) is basically a linear partial differential equation and the solution T is proportional to the absorption coefficient α, trace gas concentration c and peak pump power level P_{pump}, which all appear as coefficients of the source term of equation (1).

TABLE I
THERMAL AND OPTICAL PROPERTIES OF SILICA, CYTOP, SILICON AND AIR

Properties	Air	Silica	CYTOP	Silicon
TW/μm	UV to IR	0.2~2.2[12]	NIR[13]	1.1~6.5[12]
RI	1.0003[14]	1.47~1.43[15]	1.35~1.34[16]	3.5~3.4[17]
ρ/Kg · m^{-3}	1.205[12]	2203[12]	2030[18]	2330[12]
C_p/J · Kg^{-1}K^{-1}	1005[12]	703[12]	861[18]	714[12]
k/W · m^{-1}K^{-1}	0.026[12]	1.38[12]	0.12[18]	140[12]
TOC/10^{-6}K^{-1}	−0.91[8, 14]	9.7~8.1[15]	−50[19]	198~158[17]
TEC/10^{-7}K^{-1}	NA	4.0[20]	740[19]	26[12]

TW = transparent window, RI = refractive index, ρ = density, C_p = heat capacity, k = thermal conductivity, TOC = thermo-optic coefficient, TEC = thermal expansion coefficient, NA = not applicable.

A. Silica nano-waveguide

Fig. 3 (a) shows the simulation results for an 800-nm-diameter silica waveguide with pump modulation frequency $freq = 50$ kHz. The simulation lasts for 0.4 ms that equals 20 modulation periods, and equations (1) to (2) were used to determine the temperature distribution around the nano-waveguide. The average temperature of the surrounding gas and the waveguide increases in the first several periods and then gradually reaches a plateau, giving rise to a steady-state temperature modulation. The details of temperature evolution over two periods at steady-state is shown in Fig. 3 (b), from which the heating and cooling of the nano-waveguide in the rising and falling sides of the modulation waveform can be clearly seen. With these results and using equations (3)-(7), the normalized equivalent RI modulation due to TOE and TEE are determined and shown in Fig. 3 (c), with the amplitudes of these two contributions are $\Delta n_{TOE} = 8.15 \times 10^{-10}$ and $\Delta n_{TEE} = 0.86 \times 10^{-10}\ \mathrm{ppm}^{-1}\mathrm{W}^{-1}$, respectively. These two effects combine to give a normalized total equivalent RI modulation of $\Delta n_{Total} = 9.01 \times 10^{-10}\ \mathrm{ppm}^{-1}\mathrm{W}^{-1}$.

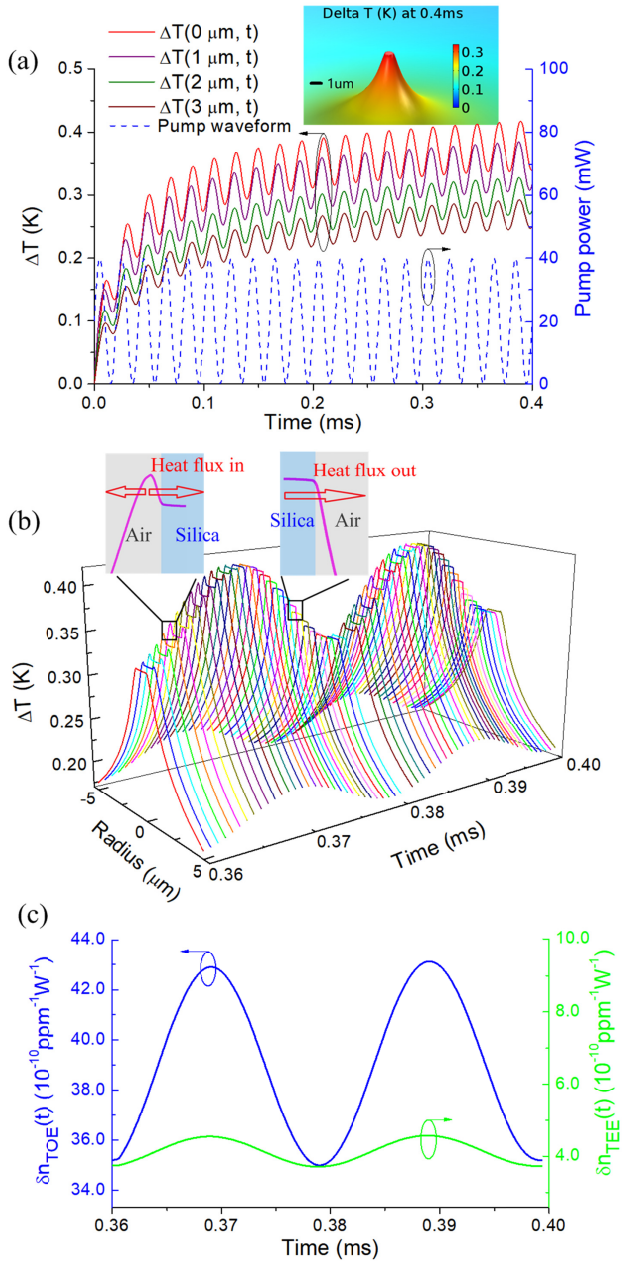

Fig. 3. Simulation results for an 800-nm-diameter silica nano-waveguide with 50 kHz modulation frequency. (a) The waveform of pump (dash line) and the evolution of ΔT (solid line) at 0, 1, 2 and 3 μm away from center of silica nano-waveguide; inset: 3D ΔT distribution at 0.4 ms; (b) Detailed evolution of ΔT distribution over two modulation periods from 0.36 to 0.4 ms; (c) Normalized equivalent RI modulation due to TOE and TEE over the two modulation periods from 0.36 to 0.4 ms

For the fixed pump modulation frequency of 50 kHz, the amplitude of the normalized equivalent RI modulation as function of waveguide diameter is shown in Fig. 4 (a). The amplitude of the total equivalent RI modulation (denoted as Δn_{Total}, the blue line) comprises of contributions from TOE (Δn_{TOE}, blue dash dot line) and TEE (Δn_{TEE}, blue dash line). The total RI modulation increases with reducing waveguide diameter, reaches a maximum at around $\sim 750\ \mathrm{nm}$ and then decreases for smaller waveguide diameter. For comparison, the normalized equivalent RI

modulation for a HC-PCF (NKT Photonics HC-1550-02 fiber) is plotted in Fig. 4 (a) as the pink dotted line, which is $-0.99 \times 10^{-10}\ \mathrm{ppm^{-1}W^{-1}}$ [6]. The RI modulation for the silica nano-waveguide with a diameter larger than ~ 550 nm is always bigger, and the maximum value that occurs around 750 nm is 9.6 times that of the HC-1550-02 fiber.

For the 800-nm-diameter silica nano-waveguide, the normalized equivalent RI modulation Δn_{Total} was also computed for pump modulation frequency from 5 to 70 kHz and the results are shown as the solid blue line in Fig. 4 (b). As expected, the amplitude of RI modulation increases with decreasing modulation frequency, giving rise to larger PT phase modulation for the probe beam and the equivalent RI modulation at 5 kHz is 5.5 times larger than that at 50 kHz

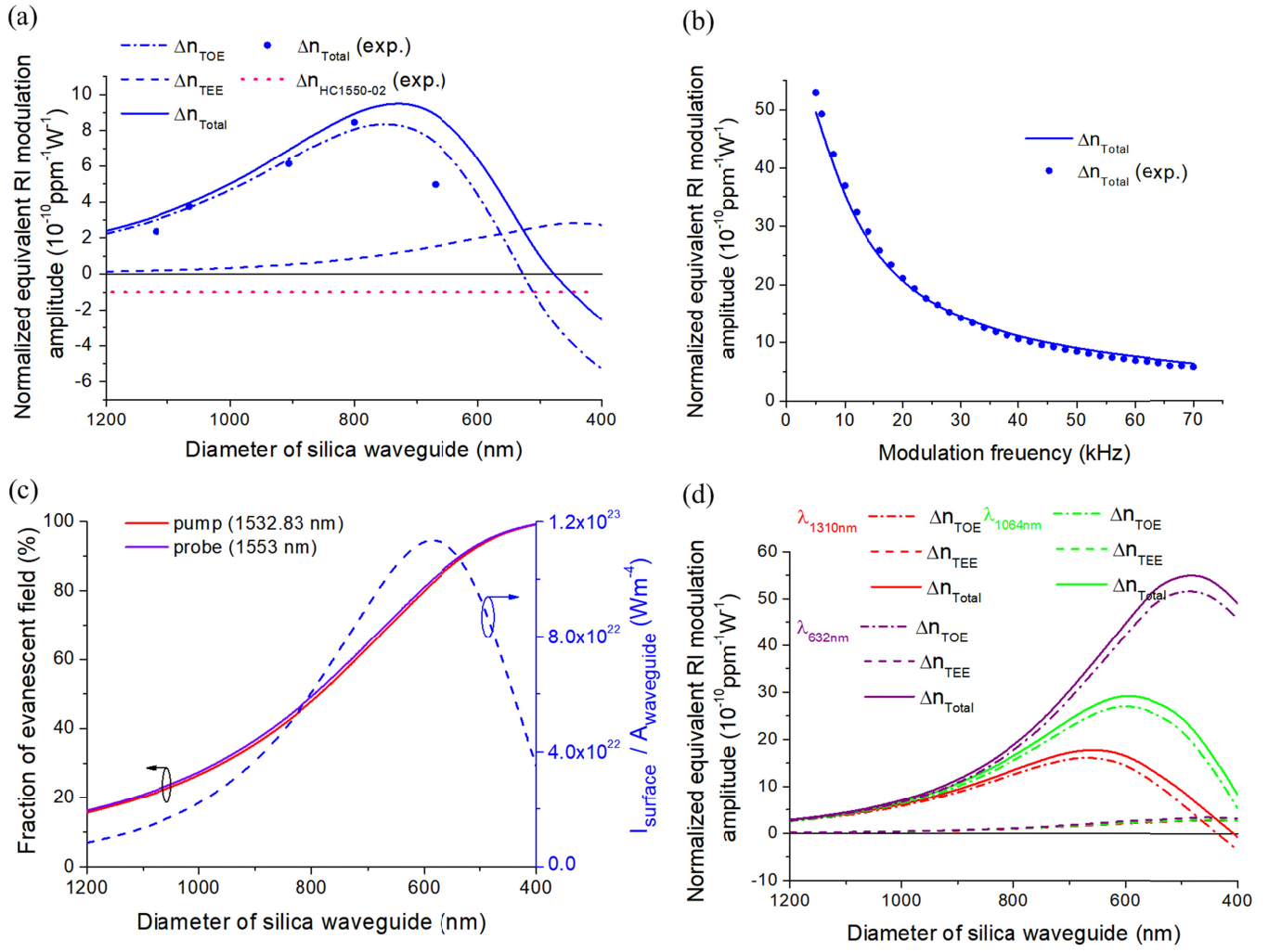

Fig. 4. Normalized equivalent RI modulation for (a) silica nano-waveguide with different diameter at fixed pump modulation frequency of 50 kHz and probe wavelength of 1553 nm; (b) 800-nm-diameter silica nano-waveguide at different pump modulation frequency with fixed probe wavelength of 1553 nm. (c) Fraction of evanescent field (for both pump and probe) and ratio of the peak-intensity of pump at waveguide surface ($I_{surface}$) over the waveguide cross-sectional area ($A_{waveguide}$) as functions of silica waveguide diameter. (d) Normalized equivalent RI modulation for silica nano-waveguide as function of waveguide diameters for three different probe wavelengths and a fixed pump modulation frequency of 50 kHz.

To understand the trend of equivalent RI modulation varying with the diameter of silica nano-waveguide shown in Fig. 4 (a), we plotted in Fig. 4 (c) the fraction of evanescent field in air as well as the ratio of the peak-intensity of pump at waveguide surface ($\mathrm{I_{surface}}$) over the waveguide cross-sectional area ($\mathrm{A_{waveguide}}$) as functions of waveguide diameter. With decreasing diameter, the fraction of evanescent field of pump (red solid line) increases, and there would be more energy to heat up the surrounding air and the silica waveguide, resulting in larger modulation of waveguide temperature. So both the Δn_{TOE} and Δn_{TEE} increase when waveguide diameter decreases from 1200 to 700 nm, as shown in Fig. 4 (a). However, further reducing waveguide diameter to below 700 nm causes Δn_{TOE} to drop instead, because the evanescent field of probe (purple solid line) in air becomes significant and the TOC of air is negative that counteracts the positive RI change of silica within which the remaining fraction of the probe light power is confined. This causes Δn_{TOE} to decrease and even reverse sign at the waveguide diameter of around 500 nm. Δn_{TEE}, which is due to

longitudinal thermal expansion of silica, continues to increase for waveguide diameter below 700 nm. Further reducing the waveguide diameter to less than 500 nm, both the decreasing rate for Δn_{TOE} and the increasing rate for Δn_{TEE} reduce, because the silica waveguide becomes too thin to tightly confine the pump beam, resulting in a substantial increase of the mode field area and dramatic decrease of the pump intensity near the surface of nano-waveguide. Considering the faster thermal conduction of waveguide as compared to surrounding air, it is the gas absorption near the waveguide surface that plays a primary role in heating up the waveguide. The blue dashed line in Fig. 4 (c) shows the ratio of $I_{surface}$ over $A_{waveguide}$ as a function of the waveguide diameter. This ratio reflects, to some extent, the capability to modulate the temperature and hence the equivalent RI of the waveguide.

As indicated above, decreasing the cross-sectional area of silica nano-waveguide increases the fraction of evanescent field of the probe beam in air, which compromises the magnitude of RI modulation due to the opposite signs of the TOCs of silica and air. This problem may be overcome by using a probe beam with a shorter wavelength so that a larger fraction of the probe power is confined in silica. This idea is demonstrated in Fig. 4 (d), in which the results for three different probe wavelengths (1310, 1064 and 632 nm) are presented. By operating the probe at 632 nm, the maximum value of the normalized RI modulation reaches Δn_{Total}=55×10^{-10} $\mathrm{ppm^{-1}W^{-1}}$, nearly 6 times bigger than the silica nano-waveguide operating at 1550 nm, and ~56 times bigger than that of the HC-1550-02 fiber.

B. CYTOP nano-waveguide

The PT phase modulation would be further enhanced by using waveguide materials with higher TOC and TEC. Generally, polymers and semiconductor materials have TOCs and TECs significantly larger than those of silica and they also have broad transparent windows in the near infrared region, as indicated in TABLE I. Fig. 5 shows the simulation results for nano-waveguides made of CYTOP. Apart from the different material properties, other parameters are the same as those used in the silica nano-waveguide simulation.

Since both the CYTOP and air have negative TOCs, Δn_{TOE} (dash dot lines) for the CYTOP nano-waveguide is always negative. With decreasing wavelength of the probe beam, the magnitude of Δn_{TOE} increases, similar to that of silica nano-waveguide. For a fixed probe wavelength, reducing the diameter of CYTOP waveguide enhances the evanescent field of the probe in air and hence Δn_{TOE} is increasingly affected by the RI change of air. At smaller waveguide diameters, Δn_{TOE} drops due to the much reduced probe light power in the CYTOP material whose TOC is about 55 times larger than that of air.

As for Δn_{TEE}, shown as the dash lines in Fig. 5, its trend is similar to that in silica nano-waveguide, i.e. with decreasing diameter, there is an initial growth (from 1200 to 600 nm) of Δn_{TEE}, which originates from the increased evanescent field of pump in air. For smaller waveguide diameter, due to dramatically decreased intensity at the surface of nano-waveguide, the heating of the waveguide is less effective and then Δn_{TEE} drops. For the CYTOP nano-waveguide, the magnitude of Δn_{TEE} is generally larger than Δn_{TOE}, resulting a positive combined total equivalent RI modulation Δn_{Total}. At the probe wavelength of 1553 nm, the maximum RI modulation is $\sim 280 \times 10^{-10}$ $\mathrm{ppm^{-1}W^{-1}}$, occurring at the waveguide diameter of ~550 nm. This value is about 29 times bigger than the silica nano-waveguide operating at 1553 nm and ~283 times bigger that of the HC-1550-02 fiber.

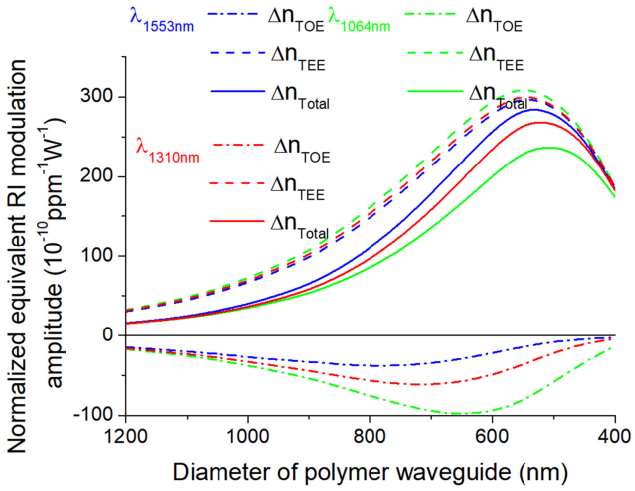

Fig. 5. Normalized equivalent RI modulation of CYTOP nano-waveguide as functions of waveguide diameter for different probe wavelengths and a fixed pump modulation frequency of 50 kHz.

C. Silicon nano-waveguide

Fig. 6 shows the simulation results for silicon nano-waveguides. The waveguide structure (shown as the inset in Fig. 6) was firstly proposed for study of interaction between photons and phonons [21]. Here, we apply this structure in PTI spectroscopy with varied silicon waveguide height from 700 to 300 nm and a fixed height-width ratio of 1.96. As the transparent window of silicon ranges from near- to mid-infrared, a pump beam with wavelength aligned to a stronger absorption line may be used to further enhance the effective RI modulation. Here we simulate the equivalent RI modulation with a pump wavelength of 3025.75 nm, corresponding to the R(9) absorption line of acetylene. It was reported that GaSe-based diode laser can operate around this wavelength under room temperature in continuous mode with output power up to 200 mW [22], which could be an ideal candidate for the pump source to improve PT RI modulation. Other parameters are the same as in silica and CYTOP waveguide simulations. Different from silica, the RI of silicon is relatively large so that for all the three probe wavelengths (1553, 1310 and 1064nm) the mode fields are all relatively tightly confined inside silicon with only a very small fraction of evanescent field experiencing the negative RI change of air. For the silicon nano-waveguide, the maximum RI modulation reaches 8100×10^{-10} $\mathrm{ppm^{-1}W^{-1}}$, about 850 times bigger than that of the silica nano-waveguide and ~8180 times of the HC-1550-02. However, it should be pointed out that the pump wavelength here is 3025.75 nm at which the absorption of

acetylene is about 24 times bigger than that at 1532.83 nm. It should also be mentioned that the heights of the silicon waveguides for single mode operation with the 1553, 1310 and 1064 nm probe are 400, 340 and 275 nm respectively, below which single mode operation is guaranteed but at the cost of lower RI modulating efficiency. The largest RI modulation occurs when the height is around 580 nm, at which the waveguide is few-mode and selective excitation of the fundamental mode is then necessary to minimize the effect of mode interference on the RI measurement.

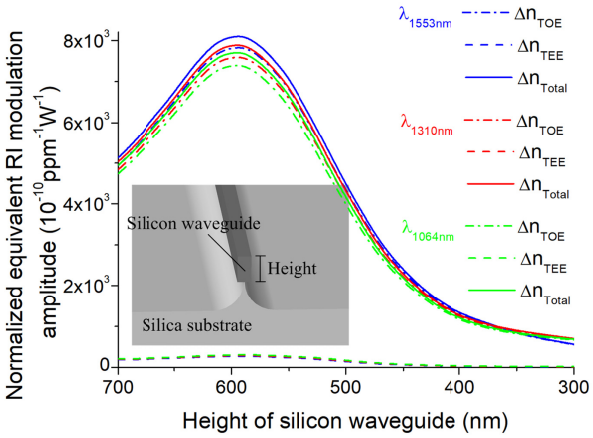

Fig. 6. Normalized equivalent RI modulation for silicon nano-waveguides with different cross-sectional size and probe wavelength at the fixed pump modulation frequency of 50 kHz. Inset: silicon nano-waveguide structure [21]. The wedge-shaped silica substrate is adopted to reduce the heat loss through the contact area between silicon waveguide and the substrate, as the thermal conductivity of silica is about 50 times larger than air. For all the simulated silicon waveguides, the width of the top of the wedge-shaped silica substrate is fixed to 20 nm.

From above simulations, what is inspiring is that by switching to nano-waveguides made of materials with higher TOC and TEC, such as polymers and semiconductors, the normalized equivalent RI modulation can be enhanced by two to three orders of magnitudes. The key properties/parameters involved in the process are TOC and TEC of the waveguide material, cross-sectional size of the waveguide and wavelength of the probe. The interplays of these parameters would determine the total equivalent RI modulation of the nano-waveguide as demonstrated above.

IV. Experiments And Results

A. Measurement of RI modulation of silica nano-waveguides

Silica nano-waveguides were taper-drawn from standard silica single mode fiber (Corning SMF-28) using the well-known flame-brushing technique [23]. All the waveguide samples are made to have the same waist length of ~12 mm, determined by the scanning range of the flame. The waist diameters of these tapered waveguides range from 670 to 1100 nm. After tapering, each of the samples is sealed into a 4-mm-bore gas cell made of Poly(methyl methacrylate) (PMMA). The single mode fiber pigtails of the sample extend to the outside of the gas cell and are used for optical connection into the measurement circuit. For the purpose of gas inlet and outlet, two side-holes were drilled near the two ends of the cell before the tapered silica nano-waveguide is housed. An image of the sealed silica nano-waveguide is shown in Fig. A1 of the Appendix.

The normalized equivalent RI modulation amplitudes of the samples were measured by a 3x3 Sagnac interferometer system and the detailed processes of measurement are shown in Section B of the Appendix. The pump light centers at the P(13) line of acetylene (1532.83 nm), with a peak power of 40 mW and an intensity modulation waveform of $g(t) = 0.5 \cdot [1 + sin(2\pi \cdot 50kHz \cdot t)]$. The wavelength of the probe is 1553 nm, at which the absorption of acetylene is negligible. The measured normalized equivalent RI modulation amplitudes for five samples of different diameters are shown in Fig. 4 (a). Comparing simulation (blue solid line) with experimental (blue dot) results, the trends of variations agree well with each other but the measured RI modulation is a bit smaller. We attribute the discrepancy to the non-uniform diameter along the waist zone [24]. For the sample with 800 nm diameter, the measured Δn_{Total} is 8.47×10^{-10} $\mathrm{ppm^{-1}W^{-1}}$, which is 8.5 times higher than that of HC-PCF measured under the same experimental conditions [6]. In addition, its normalized equivalent RI modulation amplitudes under different modulation frequency are also measured and the results are shown in Fig. 4 (b). The experimental results (blue dot) have the same tendency as the simulation results with decreasing modulation frequency.

B. Detection of trace acetylene

With the 12-mm-long, 800-nm-diameter silica nano-waveguide, trace acetylene detection experiments were carried out with the Mach-Zehnder interferometer system shown in Fig. 7. The pump source is a distributed feedback (DFB) laser with a full width at half maximum (FWHM) linewidth of 5 MHz, and its central wavelength is tuned to the P(13) line of acetylene (1532.83 nm). The probe source is an external cavity diode laser (ECDL) with a FWHM linewidth of 300 kHz, and its wavelength is fixed to 1556.59 nm where the absorption of acetylene is negligible.

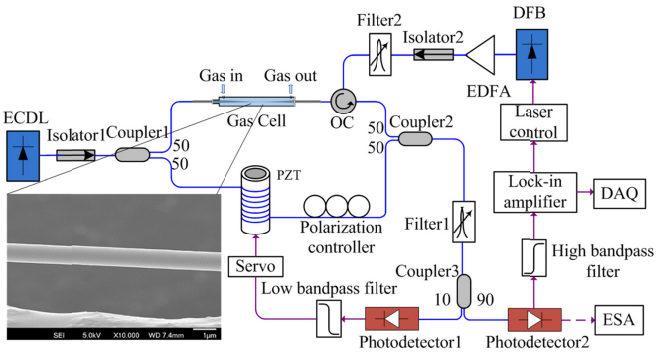

Fig. 7. Mach-Zehnder interferometer system for PT gas detection. ECDL, external cavity diode laser; OC: optical circulator; PZT, piezoelectric transducer which is used for phase stabilization; ESA: electric spectrum analyzer; DAQ: data acquisition; DFB: distributed feedback laser; EDFA: erbium doped fiber amplifier. Filter 1 centers at 1556.59 nm to block pump light; Filter 2 centers at 1532.83 nm to minimize the spontaneous emission noise from EDFA, both of them have a 3 dB bandwidth of 3 nm. Inset: Scanning electron microscopy of an 800-nm-diameter silica nano-waveguide.

The wavelength of the DFB laser is sinusoidally modulated at a frequency of 30.93 kHz via its injection current (See Section C of Appendix for the selection of wavelength modulation frequency) and the second harmonic is lock-in detected as the system output. The amplitude of wavelength modulation is selected to be ~2.2 times the line width of P(13) line to maximize the second harmonic output [25], and the nominal wavelength of the DFB is simultaneously slowly ramped across the absorption line from 1532.74 to 1532.92 nm.

Fig. 8 (a) shows the experimental results for different concentrations of acetylene (450, 525, 600 and 675 ppm) balanced by nitrogen with the pump power fixed at 50 mW. The background second-harmonic output may come from the dust attached to the silica nanofiber, which was not fabricated in a cleanroom. The PT signal (defined as the peak-to-peak value of the second harmonic output) is approximately proportional to the concentration of acetylene, as shown in Fig. 8 (b).

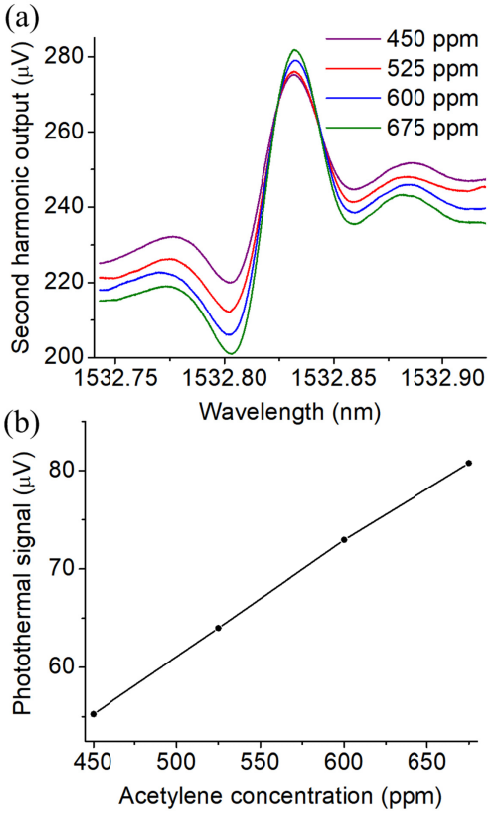

Fig. 8. (a) Second-harmonic output with pump wavelength ramping from 1532.74 to 1532.92 nm for 450, 525, 600 and 675 ppm acetylene; (b) Signal amplitude as function of acetylene concentration. The time constant of lock-in amplifier is 300 ms with a filter slope of 18 dB/Oct.

Fig. 9 shows the results of measurement for different pump power levels (22, 44, 66 and 88 mW) with a fixed acetylene concentration of 750 ppm. The PT signal increases with the pump power, as shown in Fig. 9 (c) (the blue line). The noise performance of the system was also evaluated by tuning the pump wavelength to 1532.74 nm, recording the second harmonic output as a function of time (see Fig. 9 (b)) and calculating the standard deviation (1σ value) over a period of one minute. The 1σ noise level does not change much but the PT signal increasing linearly with pump power, showing the signal-to-noise ratio (SNR) can be improved by using a higher pump power.

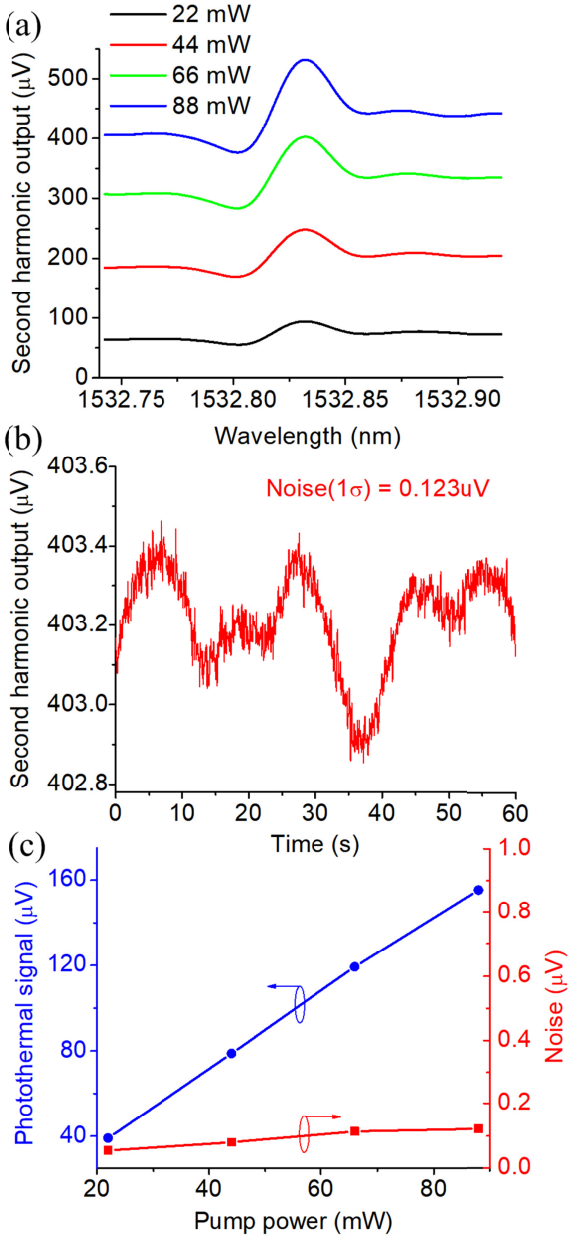

Fig. 9. (a) Second-harmonic output with pump wavelength ramping from 1532.74 to 1532.92 nm for 22, 44, 66 and 88 mW pump power; (b) Second-harmonic output over a period of 1 minute with pump wavelength fixed to 1532.74 nm and 88 mW pump power; (c) Signal and 1σ noise for 22, 44, 66 and 88 mW pump power. The lock-in amplifier time constant is 1s and filter slope is 18 dB/Oct.

The detection limit was evaluated based on the results for the 750 ppm acetylene and 88 mW pump power. The signal, 1σ noise and SNR are 155.6 μV, 0.123 μV and 1265 respectively, giving a noise equivalent lower detection limit of 600 ppb acetylene.

V. Conclusions

We have reported a nano-waveguide enhanced PTI spectroscopy method for trace molecule detection. Theoretical formulation of the method is presented and factors that affect the PT phase or equivalent RI modulation are discussed. Numerical simulation with silica, cyclic transparent optical polymer and silicon nano-waveguides shows that enormous enhancement of PT index modulation, from 10 to over 8000 times that of the commercial HC-1550-02 photonic bandgap fiber, can be achieved. Experiments with silica nano-waveguides support the numerical simulation. Gas detection experiments with 12-mm-long, 800-nm-diamter silica nanofiber demonstrated a lower detection limit of 600 ppb acetylene at ambient conditions. With CYTOP and silicon nano-waveguides of similar geometric dimensions, gas detection down to ppb and sub-ppb level would be possible. The high PT modulation coefficient and the very broad transmission of the nano-waveguide, as compared with a hollow-core photonic bandgap fiber, would enable high sensitivity multiple gas detection with a single waveguide of short length.

Appendix

A. Image of a sealed silica nanoscale waveguide

An image for a sealed silica nanoscale waveguide in PMMA tube is shown in Fig. A1:

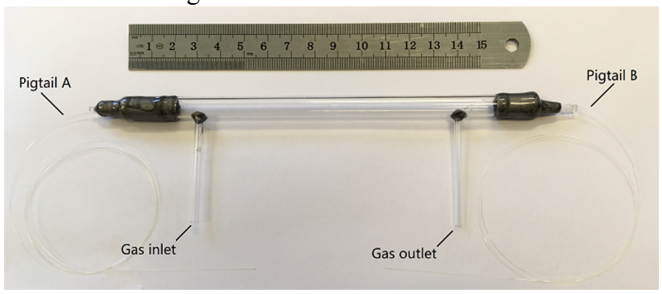

Fig. A1. Image for a sealed silica nanoscale waveguide

B. Measurement of the normalized equivalent RI modulation amplitude

The normalized equivalent RI modulation of silica nano-waveguides is measured by the 3x3 Sagnac system shown in Fig. A2 [26]. Probe light is supplied by a broadband source (BS) with center wavelength of 1553 nm. After going through the delay loop, probe light is filtered by Filter 1 and 2 whose pass band center at 1553 nm. The probe light is detected by a balanced-detector and the signal is input into lock-in amplifier. The pump light originates from external cavity diode laser (ECDL). After being amplified by EDFA and filtered by Filter 3 with pass band centering at 1532.93 nm, it is modulated by an acousto-optic modulator with modulation waveform $g(t) = 0.5 \cdot [1 + sin(2\pi \cdot freq \cdot t)]$. The peak power of pump entering into the silica nano-waveguide is fixed to 40 mW.

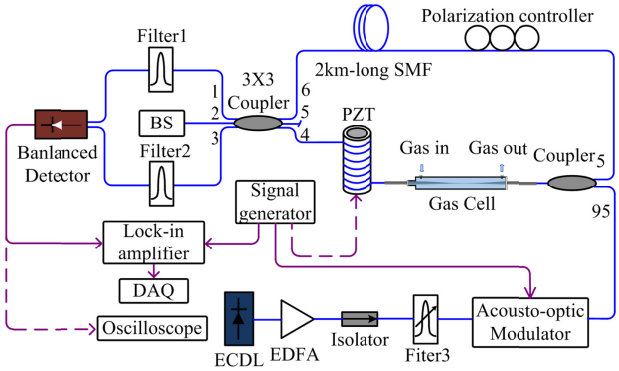

Fig. A2. Setup of the 3x3 Sagnac system. BS, broadband source. PZT, piezoelectric transducer; ECDL, external cavity diode laser; EDFA, erbium doped fiber amplifier; DAQ, data acquisition. Filter 1&2 center at 1553 nm to block pump light. Filter 3 is a tunable filter with 3dB bandwidth of 0.8 nm and centers at 1532.93 nm to block spontaneous emission noise from EDFA.

At first, pure nitrogen is inflated into gas cell and the lock-in amplifier output for 1532.83 nm pump (corresponding to P(13) line of acetylene) and 1533.03 nm pump (where absorption of acetylene is negligible) are measured as $o_{nitrogen\ at\ 1532.83nm}$ and $o_{nitrogen\ at\ 1533.03nm}$. Their difference is denoted as $\Delta s_{nitrogen}$. Then acetylene with concentration of 7500 ppm is inflated into the gas cell and the lock-in amplifier output for 1532.83 nm pump and 1533.03 nm pump are measured as $o_{acetylene\ at\ 1532.83nm}$ and $o_{acetylene\ at\ 1533.03nm}$. The difference of them is denoted as $\Delta s_{acetylene}$. The photothermal signal caused by pump absorption of 7500 ppm acetylene is obtained as $s_{acetylene} = \Delta s_{acetylene} - \Delta s_{nitrogen}$. Then the pump light is shut down for phase calibration. The PZT is driven by signal generator with waveform of $A_{PZT} \cdot 0.5 \cdot [1 + sin(2\pi \cdot freq \cdot t)]$, where A_{PZT} is the voltage amplitude and $freq$ is the modulation frequency, which is the same as the pump modulation frequency. Adjust the A_{PZT} until the output of lock-in amplifier equals to $s_{acetylene}$ and denote this A_{PZT} value as $A_{PZT\ equivalent}$. Then the actual photothermal phase modulation amplitude due to absorption of 7500 ppm acetylene is:

$$\Delta\varphi_{experiment} = \frac{A_{PZT\ equivalent}}{A_{PZT-\pi}} \cdot \pi \qquad \text{(A1)}$$

where $A_{PZT-\pi}$ is the voltage amplitude when the phase modulation amplitude of PZT equals π, which has a unique time domain waveform and can be easily discerned from the oscilloscope [27].

As an example, for the 12-mm-long and 800nm-diameter silica nano-waveguide with 40 mW peak pump power and 50 kHz pump modulation frequency, the $o_{nitrogen\ at\ 1532.83nm}$, $o_{nitrogen\ at\ 1533.03nm}$ and $\Delta s_{nitrogen}$ are 10.44, 10.42 and 0.02mV respectively. The $o_{acetylene\ at\ 1532.83nm}$, $o_{acetylene\ at\ 1533.03nm}$, $\Delta s_{acetylene}$ and $s_{acetylene}$ are 13.23, 10.04, 3.19 and 3.17mV respectively. The $A_{PZT\ equivalent}$ and $A_{PZT-\pi}$ are 22.8 mV and 5.8 V respectively. So $\Delta\varphi_{experiment}$ is evaluated to be:

$$\Delta\varphi_{experiment} = \frac{22.8mV}{5.8V} \cdot \pi = 12.34\ mrad \qquad \text{(A2)}$$

So the normalized equivalent RI modulation amplitude is:

$$\Delta n_{Total} = \frac{12.34mrad \cdot 1553nm}{40mW \cdot 7500ppm \cdot 2\pi \cdot 12mm} = 8.47 \times 10^{-10} \mathrm{ppm}^{-1}\mathrm{W}^{-1} \quad \text{(A3)}$$

C. Determination of wavelength modulation frequency in MZI system

The noise spectrum of the MZI system shown in Fig. 7 was measured using the ESA connected to Photodetector 2. The results are shown in Fig. A3. As is shown that when the PZT phase stabilizer is power on, no matter the phase stabilization function is executed or not, there is generally a much higher noise level. This is attributed to the combination of electric noise of the servo driver and the resonance characteristic of PZT. It is obviously from Fig. A3 that the noise is minimum at 61.86 kHz, with a noise level of ~2.2 dB higher than when PZT was switched off. As the second harmonic of the pump wavelength modulation is measured here, we set the modulation frequency of pump to 30.93 kHz, which is half of the minimum-noise frequency.

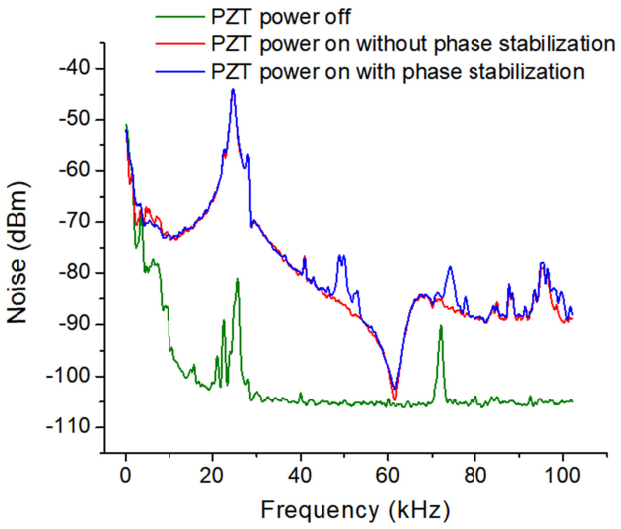

Fig. A3. Noise spectrum of the MZI system with PZT power off (green line); PZT power on without phase stabilization (red line); PZT power on with phase stabilization (blue line)

REFERENCE

[1] S. Bialkowski, *Photothermal Spectroscopy Methods for Chemical Analysis*: Wiley, 1996.

[2] C. C. Davis, "Trace detection in gases using phase fluctuation optical heterodyne spectroscopy," *Applied Physics Letters,* vol. 36, pp. 515-518, 1980.

[3] M. A. Owens, C. C. Davis, and R. R. Dickerson, "A Photothermal Interferometer for Gas-Phase Ammonia Detection," *Analytical Chemistry,* vol. 71, pp. 1391-1399, 1999.

[4] A. Sedlacek and J. Lee, "Photothermal interferometric aerosol absorption spectrometry," *Aerosol Science and Technology,* vol. 41, pp. 1089-1101, 2007.

[5] W. Jin, Y. Cao, F. Yang, and H. L. Ho, "Ultra-sensitive all-fibre photothermal spectroscopy with large dynamic range," *Nature communications,* vol. 6, 2015.

[6] F. Yang, W. Jin, Y. Lin, C. Wang, H. L. Ho, and Y. Tan, "Hollow-core Microstructured Optical Fiber Gas Sensors," *Journal of Lightwave Technology,* vol. PP, pp. 1-1, 2016.

[7] Y. Lin, W. Jin, F. Yang, J. Ma, C. Wang, H. L. Ho, *et al.*, "Pulsed photothermal interferometry for spectroscopic gas detection with hollow-core optical fibre," *Scientific Reports,* vol. 6, p. 39410, 2016.

[8] C. C. Davis and S. J. Petuchowski, "Phase fluctuation optical heterodyne spectroscopy of gases," *Applied Optics,* vol. 20, pp. 2539-2554, 1981.

[9] L. Tong, R. R. Gattass, J. B. Ashcom, S. He, J. Lou, M. Shen, *et al.*, "Subwavelength-diameter silica wires for low-loss optical wave guiding," *Nature,* vol. 426, pp. 816-819, 2003.

[10] Y. Cao, W. Jin, L. H. Ho, and Z. Liu, "Evanescent-wave photoacoustic spectroscopy with optical micro/nano fibers," *Optics Letters,* vol. 37, pp. 214-216, 2012.

[11] J. H. Lienhard, *A heat transfer textbook*: Courier Corporation, 2013.

[12] M. J. Weber, *Handbook of Optical Materials*: Taylor & Francis, 2002.

[13] K. Peters, "Polymer optical fiber sensors—a review," *Smart materials and structures,* vol. 20, p. 013002, 2010.

[14] P. E. Ciddor, "Refractive index of air: new equations for the visible and near infrared," *Applied optics,* vol. 35, pp. 1566-1573, 1996.

[15] D. B. Leviton and B. J. Frey, "Temperature-dependent absolute refractive index measurements of synthetic fused silica," 2006, pp. 62732K-62732K-11.

[16] R. Gravina, G. Testa, and R. Bernini, "Perfluorinated plastic optical fiber tapers for evanescent wave sensing," *Sensors,* vol. 9, pp. 10423-10433, 2009.

[17] G. Ghosh, *Handbook of optical constants of solids: Handbook of thermo-optic coefficients of optical materials with applications*: Academic Press, 1998.

[18] J. Gosciniak and S. I. Bozhevolnyi, "Performance of thermo-optic components based on dielectric-loaded surface plasmon polariton waveguides," *Scientific Reports,* vol. 3, p. 1803, 2013.

[19] A. Lacraz, M. Polis, A. Theodosiou, C. Koutsides, and K. Kalli, "Femtosecond Laser Inscribed Bragg Gratings in Low Loss CYTOP Polymer Optical Fiber," *IEEE Photonics Technology Letters,* vol. 27, pp. 693-696, 2015.

[20] W. H. Souder, P., "Measurements on the thermal expansion of fused silica," *Scientific Papers of the Bureau of Standards,* vol. 21, pp. 1-23, 1925.

[21] R. Van Laer, B. Kuyken, D. Van Thourhout, and R. Baets, "Interaction between light and highly confined hypersound in a silicon photonic nanowire," *Nature Photonics,* vol. 9, pp. 199-203, 2015.

[22] T. Hosoda, G. Kipshidze, L. Shterengas, S. Suchalkin, and G. Belenky, "200 mW type I GaSb-based laser diodes operating at 3 μ m: Role of waveguide width," *Applied Physics Letters,* vol. 94, p. 261104, 2009.

[23] M. Yasin, S. W. Harun, and H. Arof, *Selected topics on optical fiber technology*: InTech, 2012.

[24] T. Birks and Y. W. Li, "The shape of fiber tapers," *Lightwave Technology, Journal of,* vol. 10, pp. 432-438, 1992.

[25] J. Reid and D. Labrie, "Second-harmonic detection with tunable diode lasers—comparison of experiment and theory," *Applied Physics B,* vol. 26, pp. 203-210, 1981.

[26] K. Kråkenes and K. Bløtekjaer, "Sagnac interferometer for underwater sound detection: noise properties," *Optics Letters,* vol. 14, pp. 1152-1154, 1989.

[27] R. Bartolo, A. Tventen, C. Kirkendall, P. Juodawlkis, W. Loh, and J. Plant, "Characterization of a Low-phase-noise, High-power (370 mW), External-cavity Semiconductor Laser," DTIC Document2010.